Forecasting Remote Atmospheric Responses to Decadal Kuroshio Stability Transitions

L. SIQUEIRA,[a] B. P. KIRTMAN,[a,b] AND L. C. LAURINDO[a,c]

[a] *Rosenstiel School of Marine and Atmospheric Science, University of Miami, Miami, Florida*
[b] *Cooperative Institute for Marine and Atmospheric Studies, University of Miami, Miami, Florida*

(Manuscript received 28 February 2020, in final form 2 October 2020)

ABSTRACT: Based on observational estimates and global ocean eddy-resolving coupled retrospective initialized predictions, we show that Kuroshio Extension variability affects rainfall variability along the west coast of North America. We show that the teleconnection between the current undulations and downstream rainfall can lead to improved subseasonal to seasonal predictions of precipitation over California, and we demonstrate that capturing these teleconnections requires coupled systems with sufficient ocean resolution (i.e., eddy-resolving), especially over time scales longer than one season. The improved forecast skill is diagnosed in terms of 35 years of retrospective initialized ensemble forecasts with an ocean eddy-resolving and an ocean eddy-parameterized coupled model. Not only does the ocean eddy-resolving model show sensitivity to Kuroshio Extension variability in terms of western North America precipitation, but the ocean eddy-resolving forecasts also show improved forecast skill compared to the ocean eddy-parameterized model. The ocean eddy-parameterized coupled model shows no sensitivity to Kuroshio Extension variability. We also find near-decadal variability associated with a progression of a lower-tropospheric height dipole around the North Pacific and how these height anomalies lead to wind-driven Rossby waves that affect the eddy activity in the Kuroshio Extension with a time lag on the order of four years. This decadal-scale variability (~10 years) opens the possibility of multiyear predictability of western North American rainfall.

KEYWORDS: North Pacific Ocean; Atmosphere-ocean interaction; Climate variability; Climate prediction; Climate models; Climate variability

1. Introduction

The prediction of near-term changes in Earth's climate system, between 1 and 10 years in advance, mostly involves forecasting both the evolution of well-known modes of low-frequency ocean–atmosphere variability and the system's response to changes in external forcing. This emerging effort to predict near-term changes dovetails with extensive research into the historical and future impacts of anthropogenic forcing to better understand the physical processes associated with the climate system's response, with the ultimate goal of informing governments and society in general of the long-term risks of climate change (Meehl et al. 2000; Taylor et al. 2012; Stocker et al. 2013; Eyring et al. 2016). This marriage between near-term prediction and understanding the anthropogenically forced response is essential. The low-frequency modes of natural internal variability can heighten or lessen underlying long-term trends driven by external forcing and induce persistent, multiyear shifts in large-scale ocean–atmosphere patterns, with accompanying impacts on regional climate (Kirtman et al. 2013; Seager et al. 2015; Joh and Di Lorenzo 2017).

Near-term climate predictions largely depend on the initial oceanic conditions, although sea ice, snowpack, and soil moisture may also be relevant. The emergence of near-term climate predictions represents one of the newest challenges in climate science, bridging the gap between current operational seasonal forecasts and century-scale climate change projections. Skillful near-term climate predictions are expected to become operational (Kushnir et al. 2019) and increasingly useful for a range of applications, such as marine heatwaves and biogeochemical cycles (Bond et al. 2015; Di Lorenzo and Mantua 2016; Bif et al. 2019), climate-induced forest fire conditions (Drobyshev et al. 2016; Chikamoto et al. 2017), and drought and flood management (Swain et al. 2014; Swain et al. 2016; Wang and Schubert 2014; Seager et al. 2015).

In the North Pacific Ocean, low-frequency ocean–atmosphere fluctuations on interannual to decadal time scales are found to influence multiple components of the Earth system. These low-frequency fluctuations are usually described in terms of statistical modes of sea surface temperature (SST) such as El Niño–Southern Oscillation (ENSO) and the Pacific decadal oscillation (PDO; Mantua et al. 1997; Power et al. 1999; Chen and Wallace 2015; Santoso et al. 2017; Wills et al. 2018), the North Pacific Gyre Oscillation (NPGO; Di Lorenzo et al. 2008) in sea surface height (SSH), and their atmospheric counterparts. The atmospheric impacts associated with these low-frequency fluctuations include, but are not limited to, changes in storm tracks and wintertime temperatures, and in rainfall patterns over the western and south-central United States (Linkin and Nigam 2008; Dai 2012; Newman et al. 2016).

The nature of the ocean and atmosphere decadal variability in the North Pacific is crucial from the prediction standpoint. On the one hand, the so-called Hasselmann (1976) null hypothesis (climate noise scenario), in which the low-frequency variability arises simply by changes in the short time scale statistics of the atmospheric forcing, suggests a minimal

[c] Current affiliation: National Center for Atmospheric Research, Boulder, Colorado.

Corresponding author: L. Siqueira, lsiqueira@miami.edu

DOI: 10.1175/JCLI-D-20-0139.1

predictive skill due to the low atmospheric persistence. On the other hand, the coupled system scenario involving active ocean dynamics can further enhance the predictive skill due to the existence of midlatitude ocean–atmosphere coupling (Teng and Branstator 2011; O'Reilly and Czaja 2015).

The potential for midlatitude ocean–atmosphere coupling and feedbacks has been mainly explored in the Gulf Stream and Kuroshio–Oyashio western boundary currents (WBCs) with both WBCs displaying substantial decadal variability (Qiu et al. 2014; Siqueira and Kirtman 2016; Nigam et al. 2018; McCarthy et al. 2018). Moreover, earlier modeling studies in the North Pacific explored ocean–atmosphere feedback processes in the western boundary whereby the arrival of potentially predictable, long extratropical oceanic Rossby waves act to perturb the oceanic frontal dynamics that in turn feed back on the large-scale atmosphere driving new oceanic Rossby waves (Latif and Barnett 1994; Deser et al. 1999; Schneider et al. 2002; Qiu et al. 2007). Such ocean–atmosphere feedback would likely enhance the decadal variability of the coupled system compared to the expected under the climate noise scenario.

Although the large-scale ocean variability in the extratropics tends to fit in the null hypothesis, there is increasing evidence that the strong horizontal SST gradients and high SST variability associated with WBCs can influence the large-scale atmosphere via boundary layer dynamics [Minobe et al. 2008; O'Reilly and Czaja 2015; Ma et al. 2015, 2017; see Kwon et al. (2010) and Czaja et al. (2019) for a review of air–sea interaction studies]. Active ocean–atmosphere coupling in WBCs, unlike its passive large-scale counterpart, is mediated by boundary layer phenomena occurring over oceanic meso- and frontal scales, which eddy-parameterized and eddy-permitting coupled models are either unable or inadequate to resolve (e.g., Small et al. 2008; Chelton and Xie 2010; Bryan et al. 2010; Kirtman et al. 2012; He et al. 2018; Laurindo et al. 2019). Eddy-permitting models improve the representation of oceanic fronts and are likely to enhance the air–sea coupling and the SST-induced atmospheric response along the front (Feliks et al. 2007; Minobe et al. 2008; Feliks et al. 2011). However, this class of models tends to underestimate the ocean eddy activity (Maltrud et al. 1998; Malone et al. 2003; Marzocchi et al. 2015) and the strength of the ocean–atmosphere coupling, mostly due to differences in boundary current mean state representation (Roberts et al. 2016). A few recent studies have explicitly addressed the potential role of ocean eddies in remotely influencing atmospheric storm track and winter rainfall variability (Piazza et al. 2015; Zhou et al. 2015; Ma et al. 2017), and in influencing the physical process underpinning the decadal variability (Volkov et al. 2008; Marzocchi et al. 2015; Robson et al. 2018). Despite these findings, the extent of the role of ocean eddies in decadal prediction around the globe remains an open question.

The objective of our study is to explore further the role of mesoscale ocean phenomena in driving atmospheric variability at seasonal to decadal time scales using eddy-resolving ensemble retrospective climate forecasts in comparison with a similarly configured model with coarse 1.0° ocean and atmosphere resolution for the period between 1982 and 2016.

While most previous studies documenting decadal variability in the North Pacific have focused on the PDO, this study focuses on the analysis of multiyear dry (wet) wintertime conditions. These atmospheric conditions associated with the evolution of a near-decadal variability over the Pacific Northwest region of the United States (USPN region) happen to occur concomitantly with high (low) ocean eddy activity over the Kuroshio Extension. We disentangle the identified low-frequency atmospheric variability from the broad spectral peak on decadal time scales associated with a collection of physical processes involving ocean–atmosphere interactions in the midlatitudes, subtropics, and tropics (Newman et al. 2016). We show that this near-decadal mode and its time evolution represent a robust low-frequency atmospheric variability characterized by a slow (decadal) counterclockwise progression of a lower-tropospheric height dipole around the North Pacific. The existence of a similar atmospheric pressure dipole, termed the Pacific decadal precession (PDP), has been revealed in a few recent studies that employed an extended EOF analysis (Anderson et al. 2016a,b, 2017). The PDP explains persistent multiyear shifts in rainfall over the USPN region that occur beside those explicitly related to quasi-stationary standing wave–like structures of other fluctuations, such as ENSO and the PDO.

After describing the observational datasets and the hindcast models in section 2, we examine in section 3a the time evolution of the identified decadal mode over the North Pacific, the accompanying precipitation anomalies, and its relationship with SSH variability, especially in the Kuroshio Extension. We describe the differences in boreal winter rainfall variability between ensemble hindcasts and observation in sections 3a and 3b. The results, supported by observational analyses, are quantified in section 3b, and demonstrate that resolving the mesoscale ocean variability can significantly affect winter rainfall variability along the USPN region depending on the dynamic state of the Kuroshio Extension. Finally, section 4 summarizes the present study.

2. Data, models, and methods

a. Datasets

We use the global SSH datasets from SSALTO/DUACS altimetric mean dynamic topography produced by the Copernicus Marine and Environment Monitoring Service (CMEMS), to examine changes in the Kuroshio Extension (KE) dynamic state and its relationship with near-decadal fluctuations. To extend the time series before the satellite altimeter period, we utilize the Simple Ocean Data Assimilation (SODA3.3.1) Ocean Reanalysis (Carton et al. 2018) forced with NASA MERRA-2 reanalysis (Gelaro et al. 2017). Both datasets are available on a 0.25° lat/lon grid and cover the period from 1982 to 2016.

We use monthly wind stress, 850-hPa geopotential height, and precipitation from the MERRA-2 reanalysis on a 2/3° longitude × 1/2° latitude resolution to examine multiyear dry (wet) wintertime conditions associated with near-decadal fluctuations over the North Pacific. To evaluate the models'

retrospective forecasts, we compare their outputs against satellite-based estimates of rainfall and 850- and 250-hPa winds. The rainfall datasets used are the daily Tropical Rainfall Measuring Mission rainfall (TRMM 3B42) over the ocean and the bias-corrected NOAA CPC morphing technique blended with gauge analysis (CMORPH_BLD: Joyce et al. 2010) overland since orographic effects may contribute to changes in rainfall along the U.S. west coast. Both satellite products are distributed on a 0.25° lat/lon grid and cover the 1998–2016 period.

b. Model and initialization

The set of global retrospective forecasts of the National Center for Atmospheric Research (NCAR) Community Climate System Model version 4 (CCSM4) follow most elements of the North American Multi-Model Ensemble protocol (NMME; Kirtman et al. 2014). However, here we only consider retrospective forecasts initialized on 1 January 1982–2016, including three ensemble members for each initial condition (IC).

The initialization of the CCSM4 retrospective forecasts configured to an eddy-parameterized ocean resolution [low resolution (LR)] and an eddy-resolving ocean resolution [high resolution (HR)] follows the same approach described in Paolino et al. (2012) for the atmosphere and land, and the approach described in Kirtman and Min (2009) for the ocean and sea ice. We briefly discuss the respective procedures below.

All initial conditions are obtained from the Climate Forecast System Reanalysis (CFSR; Saha et al. 2010). We initialize the Community Atmosphere Model version 4 (CAM4) from multilevel fields of zonal and meridional winds, temperature, specific humidity, cloud fraction, cloud liquid water content, and cloud ice water content. The single-level fields used include surface pressure, surface geopotential, surface temperature, and planetary boundary layer height. The initial atmospheric data are regridded to a 0.9° × 1.25° horizontal grid for LR forecasts and to a 0.625° × 0.5° grid for HR forecasts, and further interpolated in both cases to the 26 hybrid sigma pressure levels used by CAM4.

We initialize the Community Land Model version 4.0 (CLM4) from daily fields of soil temperature, soil moisture, snow temperature, snow depth, canopy moisture, and vegetation temperature. We normalize these fields by their standard deviations and combine with the mean and standard deviation of soil climatology from 30 years of CLM4 output data, sampled after 100-yr (variance corrected) spinup. Initial data south of 60°S are set to model climatology. We use vegetation temperature and canopy initial moisture fields from a 7-day CCSM4 spinup forecast where CAM is initialized as above to produce fields influenced by the initial atmospheric state as observations are not available. The land grid resolution in CLM4 follows CAM4, and we interpolate as discussed above.

The ocean component initialization is, perhaps, most challenging and we emphasize that we do not explicitly initialize the ocean mesoscale eddies or intend to predict their evolution. The procedure to initialize the ocean component of CCSM4 involves the horizontal and vertical interpolation of the CFSR ocean data assimilation fields using a bilinear interpolation scheme, without any filtering. We use climatological data from long simulations of the LR (1° × 1° ocean grid) and HR (0.1° × 0.1° ocean grid) in regions where CFSR data are undefined concerning the CCSM4 ocean grid. We construct the initial salinity condition for CCSM4 restart by computing the normalized anomalies using both the CFSR and CCSM4 climatological and standard deviation data. Since no observational information is included in the sea ice initial conditions, those were set to the climatological monthly condition based on a long simulation of CCSM4.

c. Methods and statistical significance testing

We employed a Multichannel Singular Spectrum Analysis (M-SSA: Ghil et al. 2002; Groth et al. 2017) to extract the space–time variability related to robust decadal fluctuations from the NASA MERRA-2 reanalysis. First, we calculate the extended boreal winter (November–March) 850-hPa geopotential height anomaly (Z850a) by subtracting out the climatological mean value derived over the full analysis period (1982–2016) at each grid point. We then removed any linear trend and applied a 7–20-yr Butterworth bandpass filter (Walraven 1980) to the anomalies, analogous to the use of 30–90-day bandpass data to derive standard Madden–Julian oscillation (MJO) indices (Wheeler and Hendon 2004). We then subset the extratropical North Pacific domain from 15°–80°N and 125°E–90°W.

The principal component analysis (PCA) and truncation was performed here through a ''scree test'' on the eigenvalue spectra to obtain the signal/noise separation by inspecting the slope break of eigenvalues versus rank and the first three leading modes are initially retained. For our purposes, the PCA is also used to identify and subsequently remove the signal related to the first leading mode of low-frequency atmospheric winter variability over the North Pacific domain associated with the PDO (71% of the variance). After the removal of the PDO-related signal, we applied a multichannel singular spectrum analysis (M-SSA: Ghil et al. 2002; Groth et al. 2017) to the ''residual'' 850-hPa geopotential height anomalies. Within the M-SSA, the essential parameter is the width of the temporal lag window M, and we chose $M = 15$ years, enough to resolve the variability over the region on the time scales of interest. The number of retained eigenmodes (two accounting for 78% of the variance) and the chosen M determines the size of the lag-covariance matrix to be diagonalized, yielding eigenvectors [i.e., space–time empirical orthogonal functions (ST-EOFs)] consisting of lag sequences of maps. The projection of the data on the ST-EOFs yields the corresponding space–time principal components (ST-PCs), representing how these patterns evolve in time.

The detection of pairs of ST-EOFs (and of their corresponding ST-PCs) explaining similar amounts of variance are in phase quadrature, and with a similar period, suggests the presence of modulated oscillations. However, the occurrence of ST-EOF pairs alone is an inconclusive result for the existence of oscillations since they can also arise from finite samples of some nonoscillatory processes, such as first-order autoregressive (AR1) noise. Therefore, we follow the procedure designed by Allen and Robertson (1996) to test whether the oscillatory modes identified by the M-SSA correspond to

real oscillations. In this procedure, confidence intervals for a given significance level are estimated using Monte Carlo simulations, where a large ensemble (1000 members) of normally distributed surrogate noise time series is created with the null hypothesis characteristics, and yielding the same length, variance, and temporal lag-one autocorrelation as the original time series. The confidence intervals can be computed in two different ways: first, using the ST-PCs and ST-EOFs of the data, and second using the ST-PCs and ST-EOFs of the null hypothesis. In the first case, the lag-covariance matrix is computed from the data, whereas the lag-covariance matrix in the second is computed from the surrogate data generated by the Monte Carlo simulations. The subsequent procedure of projecting data and noise surrogates onto the vector basis is similar in both cases. The latter yields a more robust test, while the former implicitly assumes the existence of a signal before any signal has been identified. Finally, the projection of the data on the vector basis allows the subsequent variance examination for values higher than expected under the red noise null hypothesis, occurring at a given (dominant) time scale.

We estimate the statistical significance of the composite analysis by applying a two-sided Wilcoxon rank-sum test. Our main reason for choosing this test is that it is a nonparametric alternative to the two-sample t test, with no requirement on the distribution, and is based solely on the order in which the data from two samples fall. The fact that the test is nonparametric is of particular relevance for testing differences in rainfall composites as the rainfall distribution is non-Gaussian. For the retrospective forecast data, we concatenate the ensemble members at each grid point, and test the median values of the two distributions to check if they are significantly different (Fay and Proschan 2010; Ma et al. 2015).

3. Results

a. *Low-frequency atmospheric signatures and Kuroshio dynamic state*

The subsequent analysis focus on the sources and physical processes giving rise to multiyear dry (wet) conditions over the USPN region, targeted to the region's water availability.

To pinpoint potential sources of near-term ocean–atmosphere predictability, we employed the M-SSA analysis (cf. section 2b) to extract the space–time structure from the NASA MERRA-2 reanalysis. We identified a pair of ST-EOFs in the Z850a spectrum, and corresponding ST-PCs that emerge above their upper significance level (0.05) and explain the largest fraction of the 7–20-yr bandpass filtered winter Z850a variance (39% and 38%). The first two Z850a ST-PCs estimated by M-SSA are found to be in quadrature (not shown), indicating the presence of an oscillatory ST-EOF pair with a period of ~11 years (Fig. 1).

The time evolution of the precipitation and 850-hPa height anomalies associated with the identified near-decadal variability of the extended winter season (November–March) is shown by lead–lag regression fields in Figs. 2a–f. During anomalously dry (from years −6 to −2) and wet (from years +2 to +6) periods over the USPN region, a Z850a dipole pattern is found to slowly (on a decadal time scale) evolve

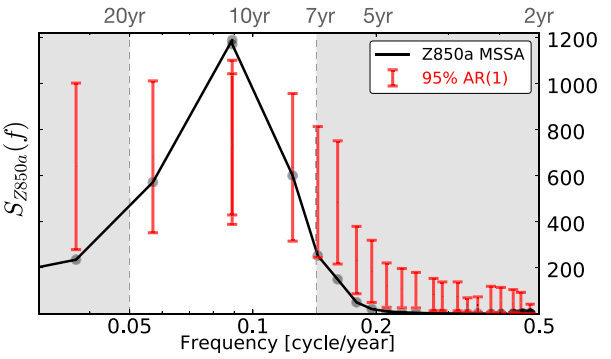

FIG. 1. Spectral properties of the detrended 7–20-yr bandpass filtered 850-hPa geopotential height anomalies in the extratropical North Pacific (15°–80°N, 125°E–90°W), using M-SSA with a window width of 15 years. The estimated variance in each mode as a function of their corresponding frequency is shown as black circles. Error bars correspond to the 5% and 95% quantiles from a Monte Carlo test (ensemble of 1000 members) for the red noise null hypothesis.

counterclockwise around the extratropical North Pacific. The existence of a similar lower-tropospheric height dipole and its evolution has been revealed in a few recent studies employing a different approach (Anderson et al. 2016a,b, 2017; Anderson 2019). Unlike these previous studies, here the identified M-SSA oscillation is termed Pacific decadal progression (PDP) due to its quasi-decadal periodicity and prograde motion around the North Pacific (Fig. 2).

In the years leading up to persistent dry conditions over the USPN region, the dipole displays a pronounced zonal orientation (Fig. 2a) with higher than average Z850a over the central subtropical North Pacific and lower than usual Z850a over Alaska [North Pacific Oscillation (NPO)-type pattern; Linkin and Nigam 2008]. As time evolves, the dipole pattern rotates counterclockwise and progressively acquires a meridional orientation as its easternmost lobe extends across the coast of western North America during the midpeak drought period (Figs. 2b,c). During the peak dry years (Fig. 2c), positive large-scale Z850a are found off the coast of western North America, characterizing a multiyear persistence of wintertime anomalously high atmospheric pressure (Anderson et al. 2016b). In our results, this anomalous ridge is part of the broad basin-scale Z850a dipole displaying a coherent spatial and temporal signature that progresses counterclockwise on the near-decadal time scale. The Z850a dipole pattern then turns back into a zonal orientation but of opposite sign in the years following the drought (Fig. 2d), eventually reverting to a meridional orientation of opposite sign concurrent with the peak of persistent wet conditions over the USPN region (Figs. 2e,f).

We further explore the relationship between the identified M-SSA mode and the low-frequency changes in SSH anomalies (SSHa), mostly concentrated along the Kuroshio Extension (KE) region of 31°–36°N, 140°–165°E. This region encompasses both the time-mean eastward flowing KE jet and its southern recirculation gyre, the most variable circulation feature in the

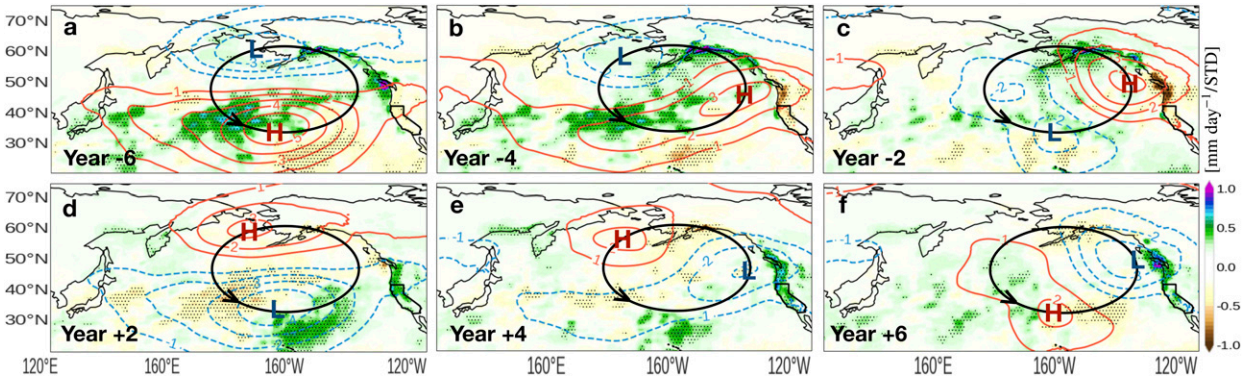

FIG. 2. Lag regression of boreal winter (November–March) rainfall [shaded; mm day^{-1} per standard deviation (STD)] and 850-hPa geopotential height anomalies (contours; m per STD) onto the M-SSA reconstructed time series of the PDP. Stippling indicates regression coefficients exceeding the $p < 0.10$ significance level based on a two-tailed Student's t test.

North Pacific, and is also where the largest air–sea exchanges of heat and moisture take place (Kelly et al. 2010).

From a climate noise perspective, low-frequency variability in the midlatitude ocean arises simply by interannual or interdecadal changes in the white noise atmospheric forcing. These changes may produce apparent oscillatory behavior over finite time windows merely because of accidental swings with a certain period and sampling issues [the so-called Hasselmann (1976) null hypothesis]. Although the climate noise theory has shown its usefulness in understanding the overall shape of midlatitude SST spectra (e.g., the PDO time series), this theory fails to capture the decadal spectral peak that stands out in the KE observed SST (Qiu et al. 2007). Previous studies indicate that decadal variability in regional SST, ocean heat content, and eddy activity are mostly due to transitions in the dynamic state of the KE jet (Qiu and Chen 2005; Taguchi et al. 2007; Ceballos et al. 2009).

The low-frequency variations of the KE system can be concisely represented by constructing a KE index based on the SSHa signals in the 31°–36°N, 140°–165°E region (Qiu et al. 2014). Here, we employ the KE index as a proxy to four dynamic properties, namely, the upstream KE path length, strength of the jet, latitudinal position, and strength of the recirculation gyre. By definition, a positive KE index represents a stable dynamic state in which the KE jet is strengthened with a steady and northerly path, the southern recirculation gyre is enhanced, and eddy activity is reduced. The opposite effect occurs when the KE jet switches to an unstable dynamic state (negative KE index).

The time evolution, reconstructed using the leading ST-PC pair, of the dominant wintertime 850-hPa geopotential height anomalies in the North Pacific from 1982 to 2018 is shown in Fig. 3 together with the 7-yr low-pass KE index based on November–March satellite-observed SSHa from 1993 to 2016. We extend the KE index time series for as long a period as possible using SSHa from the SODA ocean reanalysis for 1982–2016 to enhance the statistical confidence of the composite analysis in section 3b.

During the past three decades, the KE system is considered to be in a stable dynamic state during the periods 1988–93, 2002–05, and 2010–12 and unstable during 1984–86, 1995–99, and 2006–09 (Fig. 3). Selected years of negative KE index and intense eddy activity, are shown in blue and termed active eddy years (AEY), while periods of positive values and subdued eddy activity are shown in red and named inactive eddy years (IEY). The selection of the eddy active and inactive years follows the Kuroshio unstable and stable periods mentioned above, but only the years with a near-neutral phase of ENSO and PDO are considered for the composite analysis in section 3b.

It is apparent from the lagged cross-correlation between the PDP and KE indices (Fig. 4) that the 850-hPa height dipole

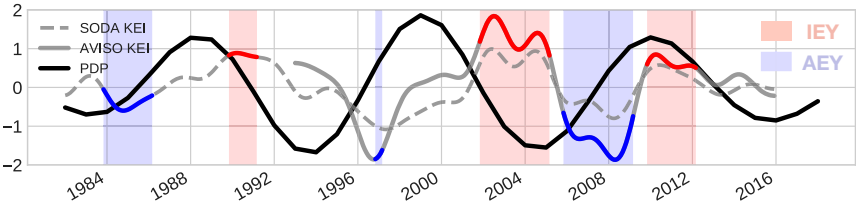

FIG. 3. Time evolution of the Pacific decadal precession (PDP) from 1982 to 2016 based on the leading M-SSA components (solid black) and the 5-yr low-pass Kuroshio Extension index (KEI) for AVISO satellite (solid gray), and SODA reanalysis (dashed gray). Both the PDP and KE indices have been normalized by their respective standard deviations. Active eddy years (AEY) are shown in blue and inactive eddy years (IEY) in red.

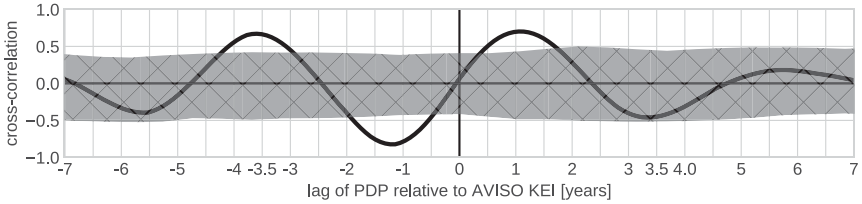

FIG. 4. Lagged cross-correlation between November–March PDP time series and the AVISO KE index. Negative (positive) years indicate the PDP index leading (lagging) the KE time series. The one-tailed (95%) significance threshold for the cross-correlation is depicted by the hatched area and estimated using the nonparametric random phase method (Ebisuzaki 1997).

typically leads the dynamical state of the KE system by about 3–4 years. Results from previous studies also indicate that the low-frequency transitions in the dynamic state of the KE system are predominantly driven by the arrival of large-scale Rossby waves that were forced by atmospheric variability about 3–4 years earlier in the central and eastern North Pacific (Seager et al. 2001; Schneider et al. 2002; Taguchi et al. 2007; Qiu et al. 2014). Moreover, a coupled feedback has been proposed (Qiu and Chen 2005; Qiu et al. 2014) whereby the delayed arrival of long oceanic Rossby waves perturbs the KE system dynamics, which in turn feed back on the large-scale atmosphere (NPO-type pattern), eventually driving new oceanic Rossby waves directed to the KE region. This delayed feedback mechanism would likely enhance the KE variability on decadal time scales and establish an essential basis for near-term predictions (Anderson 2019).

Figure 5 depicts the evolution of the 7–20-yr bandpass SSHa and Z850a associated with PDP. Positive SSHa (excited by wind stress curl) are produced by higher than average Z850a over the central subtropical North Pacific (Fig. 5a). These positive SSHa signals, guided by the KE jet, slowly propagate westward and reach the KE region (Sasaki and Schneider 2011; Sasaki et al. 2014) about four years later, as the Z850a dipole rotates counterclockwise (Figs. 5b,c). Once the SSHa crosses the date line, the extent of the anomaly narrows considerably as it approaches the KE region (Figs. 5a,b,d,e), consistent with the transition from large-scale, linear Rossby wave dynamics to mesoscale, nonlinear Rossby wave dynamics along a jet (Sasaki and Schneider 2011; Sasaki et al. 2014; Anderson 2019). Moreover, Fig. 6a suggests an increase in the phase speed of the SSHa following this transition (Sasaki et al. 2014). After the dynamic state of the KE system becomes stable (Fig. 5c), the cycle evolves to a lower than average Z850a at the central and eastern basin (Figs. 5d,e), which generates SSHa of the opposite sign, initiating the sign reversal via Rossby wave propagation. Eventually, the wind-induced negative SSHa signals propagate westward into the KE region after about four years (Fig. 5f) and switch the phase of the KE dynamic state, resulting in a negative KE index (Fig. 3). After the dynamic state of the KE system becomes unstable (Fig. 5f), the sequence of processes with an opposite sign takes place (Figs. 5a–c). This interpretation based on lead–lag regressions is further supported by a Hovmöller analysis shown in Fig. 6 for the two transects depicted as dotted lines in Fig. 5.

Figure 6 shows the time–longitude plot of the detrended 7-yr low-pass satellite-observed SSHa (Fig. 6a) along 33°N and across the North Pacific Ocean from 141°E to 150°W, and from 33°N, 150°W toward the northeast North Pacific (50°N, 140°W) in Fig. 6c (the paths are indicated in Fig. 5). Here, the influences of both the PDO (Trenberth and Hurrell 1994) and ENSO (Ropelewski and Jones 1987) indices have been removed using least squares regression. The slow Rossby wave propagation, excited by the anomalous wind stress curl in the central-eastern part (Figs. 6a,b), leads to large-scale decadal

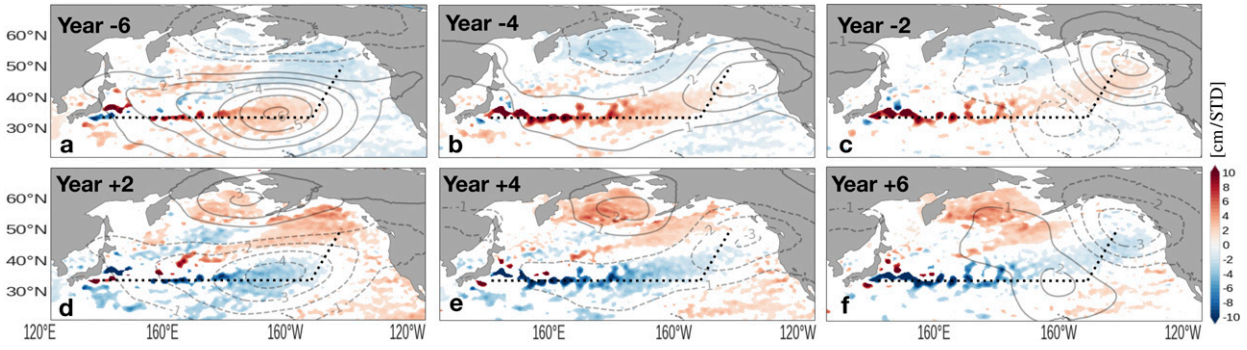

FIG. 5. Lag regression of boreal winter (November–March) SSHa (shaded; cm per STD) and 850-hPa geopotential height anomalies (contours; m per STD) onto the M-SSA reconstructed time series of the PDP. Colored areas denote regression coefficients exceeding the $p < 0.10$ significance level based on a two-tailed Student's t test. Dotted lines denote the transects used in the time–longitude plot in Fig. 6.

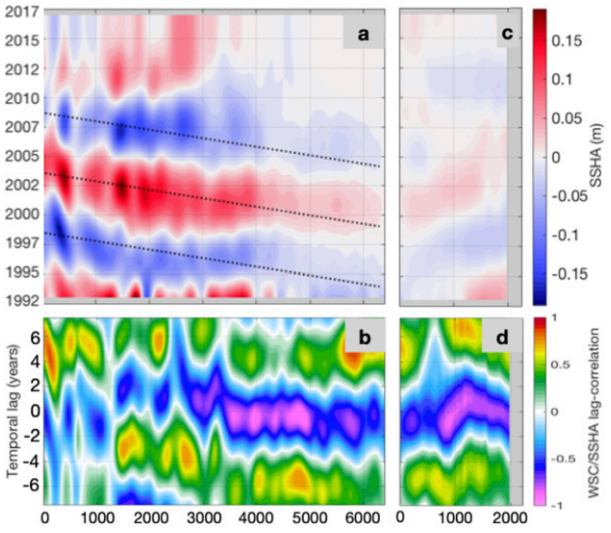

FIG. 6. Time–horizontal distance diagram for (a),(b) 33°N in the North Pacific Ocean extending from the coast of Japan to 150°W and (c),(d) from 33°N and 150°W toward the northeast North Pacific at 50°N, 140°W for the detrended 7-yr low-pass satellite-observed sea surface height anomalies in (a) and (c). The projection of the PDO and ENSO indices was removed using least squares regression. The dotted line marks a westward phase speed of 4.2 cm s^{-1}. The lagged cross-correlation between wind stress curl anomalies from MERRA-2 reanalysis and SSHa is shown for each transect in (b) and (d).

SSHa changes in the KE region (from ~0 to 3000 km). These changes are illustrated in Fig. 6a by the positive SSHa in 1992–95, 2001–05, and 2010–12 and negative SSHa in 1995–99 and 2006. Figures 6c and 6d, showing the SSHa along the northeastward transect, depict the evolution of PDP dipole as it extends across the western coast of North America (Fig. 5).

The lagged cross-correlation between the SSHa and the anomalous wind stress curl along the two transects is shown in Figs. 6b and 6d. Considering the speed of baroclinic Rossby waves (4.2 cm s^{-1}) across the latitude band from 31° to 36°N (Fig. 6a) and the lagged correlations in Fig. 6b, our results suggest that SSHa signals, produced by the low-frequency wind forcing in the eastern part of the basin, propagate westward and into the KE region in about four years. For periods longer than four years, the wind stress curl and SSHa lagged correlations display positive values at about −6 years in the central-eastern basin (Fig. 6b), indicating that the wind stress curl there might serve as a leading predictor to changes in the KE index. This lagged correlation on longer leads has been investigated by Qiu et al. (2014) while exploring the predictive skills of the KE index under a Rossby wave adjustment scenario with and without wind feedback. They report that the inclusion of the feedback Ekman pumping forcing along 31°–36°N can increase and extend the predictive skill of the KE index to a lead time of 6–7 years.

b. Winter rainfall and KE eddy activity

In this section, we first evaluate the rainfall variability over the 3-month lead times [January–March (JFM)] of the CCSM4 LR (parameterized ocean eddy version) and HR (resolved ocean eddy version) retrospective forecasts from 1982 to 2016, before examining the effect of the KE dynamical state on the rainfall over the USPN region. Although the impact of better resolving mesoscale ocean features cannot be distinguished from intrinsic differences between the 0.5° and 1° atmospheric horizontal resolution employed in our retrospective forecasts, previous results suggest that (sufficiently) higher atmospheric resolution leads to more intense vertical velocities, moisture flux, and atmospheric transient eddy heat flux responses over ocean frontal areas (Smirnov et al. 2015).

Figure 7 shows a comparison of the JFM daily rainfall mean and standard deviation simulated in LR and HR retrospective forecasts and the observational estimates over the same period. In the observational estimates, the maxima in daily rainfall are found collocated with the path and extension of the Kuroshio and in the central-eastern part of the North Pacific (Fig. 7c). The overall pattern and the position of the observed daily rainfall variance are well reproduced in both HR (Fig. 7a) and LR (Fig. 7a). However, we notice substantial improvements in the HR retrospective forecast over the WBCs along the path and extension of the Kuroshio and Gulf Stream, especially near the eastern U.S. seaboard, as well as a modest improvement in the Gulf states region toward the observed values (Figs. 7b,c). Figure 8 shows the precipitation histograms and cumulative distribution functions (CDFs) over the WBCs indicating that up to about 10 mm day^{-1}, both models overestimate the occurrence of weak and moderate events compared to observations and underestimate for larger values (Fig. 8a). For extreme values (97.5%) in the CDFs (Fig. 8b), the HR forecast shows slightly higher rainfall values than the LR. Although HR shows the improvements mentioned above compared to LR, HR-simulated standard deviations and extreme rainfall are a great deal less than observed. Overall, these model results are in agreement with Covey et al. (2018), which suggests that the CMIP5 climate models that provided high-time-frequency output, in general, underestimate the variance of daily means.

It is apparent from Figs. 2, 3, and 5 that dry (wet) periods over the USPN correspond to stable (unstable) periods of the KE dynamical state. In the subsequent analysis, we further explore this observational evidence, which points to a relationship between the dynamic state and mesoscale variability of the KE region and the winter precipitation along the USPN region. Here, we follow the approach outlined in Ma et al. (2015) by separately considering periods where the KE system is in a stable dynamic state and the eddy activity is reduced (IEY) and periods where the eddy activity is relatively large (AEY) and the KE system is in an unstable state. Based on the results from Fig. 3, the seven AEY cases include January–March of 1984, 1986, 1997, and 2006–09, and the IEY cases occur in 1990, 1991, 2002–05, and 2010. In particular, we will explore the potential atmospheric response when accounting for ocean meridional shifts of the KE jet and its associated mesoscale variability, driven by decadal changes in the KE system state in low- and high-resolution ensemble retrospective forecasts.

The low- and high-resolution retrospective forecasts were initialized on 1 January for each year, including three-member ensembles, and the first 90 days of the forecast are considered.

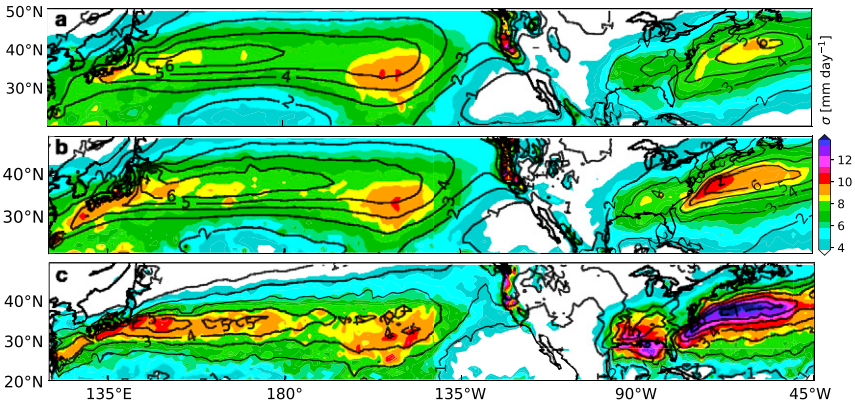

FIG. 7. January–March daily rainfall mean (contours) and standard deviation (shading) from 1982–2016 over the Pacific–North American sector: (a) LR (global coupled low-resolution retrospective forecast), (b) HR (global coupled high-resolution forecast), and (c) observation (TRMM 3B42 and CMORPH_BLD).

Due to the shortness of the satellite-based rainfall data, we consider five AEY (1997 and 2006–09) and IEY (2002–05 and 2010) for the observational estimates.

Figures 9a–c summarize the effect of the KE mesoscale activity in terms of the January–March mean rainfall difference between composites based on inactive (stable) eddy years and active (unstable) eddy years (IEY − AEY) in observational estimates (Fig. 9a) and the ensemble average of the retrospective forecasts (Figs. 9b,c). The difference between the composites indicates an increase in rainfall in the USPN region, especially over central-northern California, when the eddy activity is reduced (IEY), and the KE system is stable (Figs. 9a,b). The HR retrospective forecast captures this difference (Fig. 9b), with amplitudes comparable to observations (Fig. 9a). In contrast, the LR forecast displays a stronger decrease in rainfall over the northern part of the USPN (Fig. 9c) and a much weaker (nonsignificant) increase over southern California.

Figure 10 shows the observed and ensemble average hindcasts for the difference IEY − AEY in daily rainfall over land and the individual CDF, specially targeted to California's water availability. Here we employ both the Kolmogorov–Smirnov statistic to quantify the distance between the empirical cumulative distribution functions of the two samples and the Dvoretzky–Kiefer–Wolfowitz inequality (Dvoretzky et al. 1956) for generating CDF-based confidence bounds and producing a confidence band at the 90% confidence level.

Clearly, the LR forecast shows a weaker and dipolar spatial pattern (Fig. 10c) and does not capture differences in the daily rainfall distribution between the active and inactive eddy years. The differences in rainfall are accentuated in the HR forecasts (Fig. 10b), but reproduce well the observed spatial pattern (Fig. 10a), showing a robust difference in the daily rainfall distributions (Fig. 10b). In the HR case, for example, only 23% of the AEY make more than 5 mm per day compared to 34% of the IEY; from another perspective, there is a robust shift of the 25%, 50%, and 75% percentile toward higher values in the IEY (Fig. 10b). In the observations, there is a barely significant difference at the 75% percentile, although differences are also seen at 97.5% extreme values (Fig. 10a).

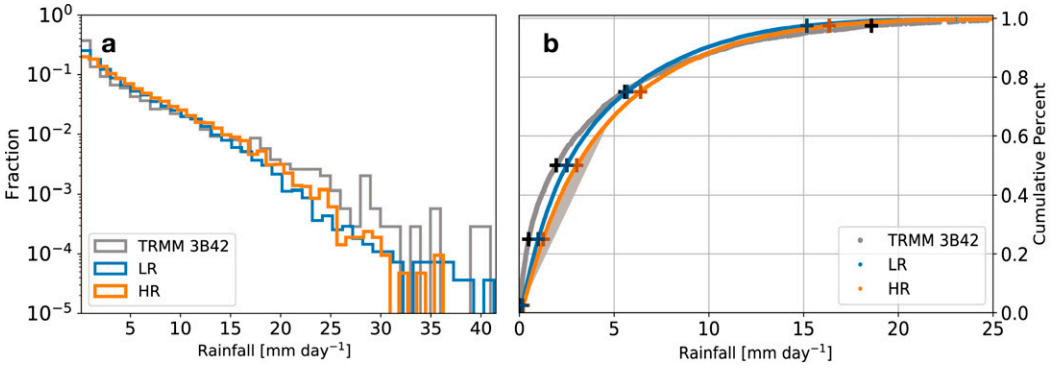

FIG. 8. (a) Probability distributions of daily precipitation in the Kuroshio (30°–38N, 125°–155°E) and Gulf Stream systems (32°–40°N, 78°–48°W) aggregated in 1 mm day^{-1} bins from 0 to 40 mm day^{-1}. (b) Daily rainfall empirical CDFs, where crosses display the location of the 2.5th, 25th, 50th, 75th, and 97.5th percentiles from left to right.

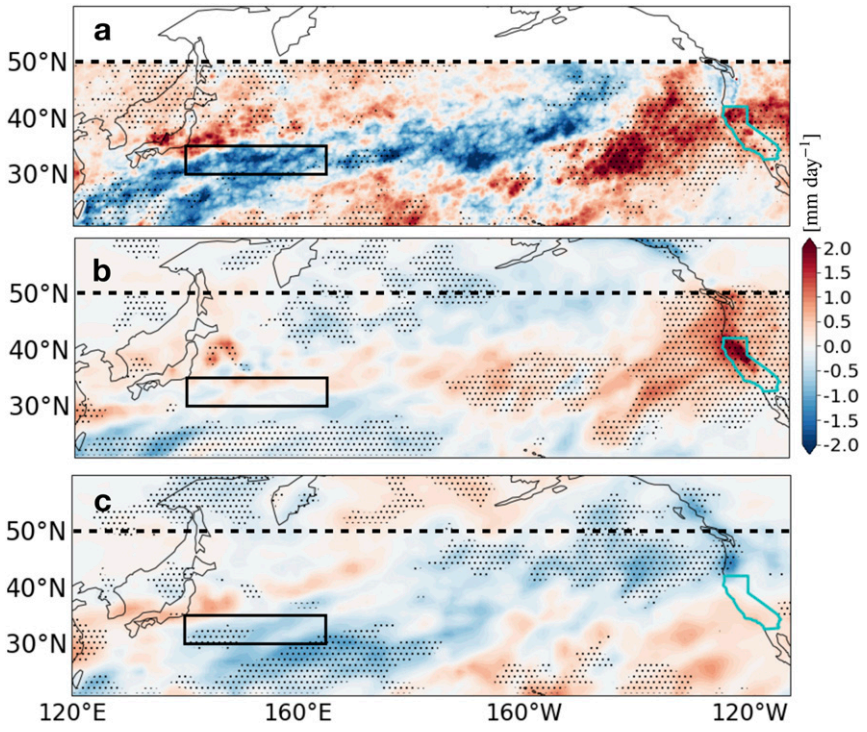

FIG. 9. Difference in January–March rainfall composites between inactive eddy years (IEY) and active eddy years (AEY) for (a) TRMM 3B42 (5 years each), (b) ensemble average HR retrospective forecast (7 years each), and (c) ensemble average LR retrospective forecast (7 years each). IEY and AEY are taken from observational estimates in Fig. 3a. Rainfall difference significant at 95% confidence level based on a two-sided Wilcoxon rank-sum test is shaded by dots.

Although we do not find a robust shift in the percentiles for the observations, the Kolmogorov–Smirnov statistic suggests that the distance between the CDFs of the AEY and IEY is robust (p value is less than 0.05).

In the KE region, the SST anomalies shown in Figs. 11a and 11b emerge after the arrival of PDP-induced oceanic Rossby waves and corresponding SSHa (Figs. 5b,e) and are accompanied by a substantial transfer of heat to the overlying atmosphere via surface turbulent heat fluxes in the Kuroshio–Oyashio confluence region (Figs. 11c,d) in the IEY and AEY composites. Here we focus only on turbulent heat flux anomalies that are positively correlated with the underlying SST anomalies during the considered IEY and AEY periods (Figs. 11e,f), linear relationship that is indicative of a thermodynamic oceanic forcing of the atmosphere (Wu et al. 2006; Kirtman et al. 2012; Bishop et al. 2017; Small et al. 2019). The turbulent heat fluxes induced by the SST fluctuations in the KE region can subsequently induce remote atmospheric pressure anomalies and circulation patterns over the eastern North Pacific on subseasonal and longer (beyond seasonal) time scales. At subseasonal time scales, localized heat fluxes modify the baroclinicity of the atmosphere, which in turn modulates the growth rate and energy transport of baroclinic storms in the region (Rivière 2009; Ma et al. 2015; Révelard et al. 2016; Ma et al. 2017; Sugimoto et al. 2017), while at the longer time scales the time integration of the anomalous baroclinic eddy activity results in an equivalent barotropic atmospheric response (O'Reilly and Czaja 2015; Ma et al. 2015; Révelard et al. 2016; Ma et al. 2017). Figures 12a and 12b show the difference in geopotential height anomalies at 250 and 850 hPa between IEY and AEY composites, where the upper- and lower-level winter mean geopotential height anomalies display an anomalous equivalent barotropic circulation in the North Pacific. These are consistent with the southward shift of the upper-tropospheric storm track and zonal wind in the eastern North Pacific (Fig. 12) and corresponds to the dipole-like response in upper-level storm track activity (Figs. 12e,f) with an increase (decrease) in storm activity to the south (north) of the jet stream in the eastern North Pacific.

Based on empirical analysis, Anderson (2019) suggests an extratropical tethered pathway in which the KE variability plays a vital role. In this view, the PDP forces the atmospheric circulation that generates the westward propagating Rossby waves that can subsequently modify the KE state. In contrast, the KE mesoscale ocean–atmosphere coupling induces remote atmospheric pressure anomalies over the eastern North Pacific of opposite sign, setting the stage for the opposite phase of the PDP cycle.

To examine the possibility that the SST and corresponding heat flux anomalies in the KE region may be, in part, responsible

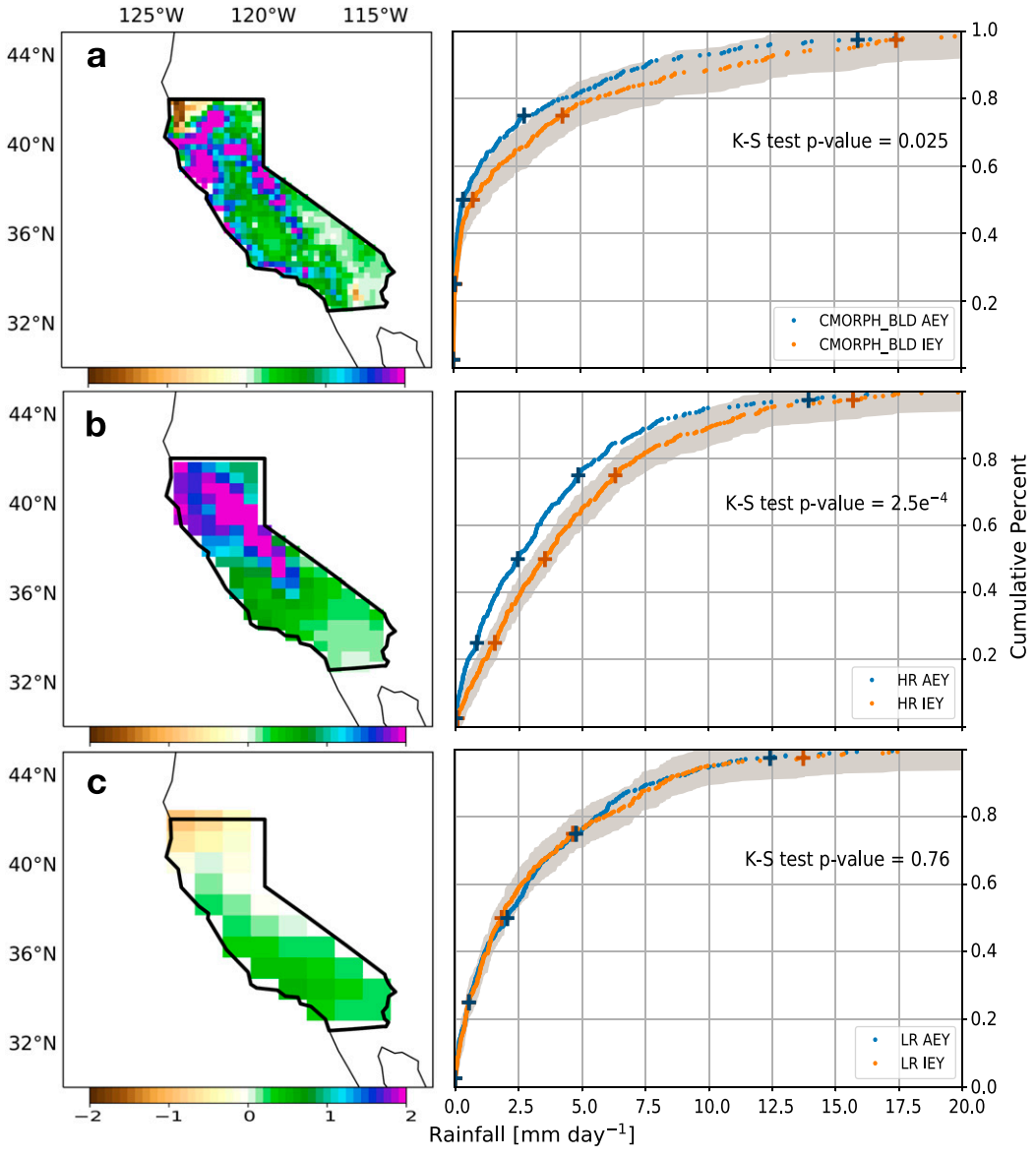

FIG. 10. (left) The difference in January–March daily rainfall between inactive eddy years and active eddy years (IEY − AEY) for (a) CMORPH_BLD, (b) HR, and (c) LR retrospective forecasts (mm day^{-1}). (right) As in the left panels, but for daily rainfall empirical CDFs for IEY (orange) and AEY (blue) over California. The shaded area in the right panels denotes the confidence band at the 90% confidence level based on the Dvoretzky–Kiefer–Wolfowitz inequality (Dvoretzky et al. 1956).

for the development of the atmospheric circulation patterns over the eastern North Pacific, we investigate the KE downstream atmospheric response by calculating the correlation maps of the KE index with the wind stress curl anomalies for a lag of 2 months (Fig. 13). The KE's feedback to the atmosphere shown in Fig. 13 agrees with several observational studies (Frankignoul et al. 2011; Qiu et al. 2014; Na et al. 2018; Joh and Di Lorenzo 2019) that investigate the downstream atmospheric and oceanic response to the KE stable state, showing positive wind stress curl anomalies consistent with a cyclonic atmospheric response in the subtropical eastern Pacific. In our results, the KE's downstream atmospheric response in Fig. 13 does not effectively project on the forcing pattern for the KE variability but is more consistent with the Pacific meridional mode forcing pattern by weakening the trade winds in the subtropical eastern Pacific (Joh and Di Lorenzo 2019).

Given the possibility that the KE state may be important for determining the nature of the North Pacific storm track, let us now turn our attention to the lower- and upper-level storm-track changes in the HR ensemble forecast. Figures 12c–f show the difference in January–March 850-hPa and 250-hPa mean zonal winds and the storm track represented using the 250-hPa

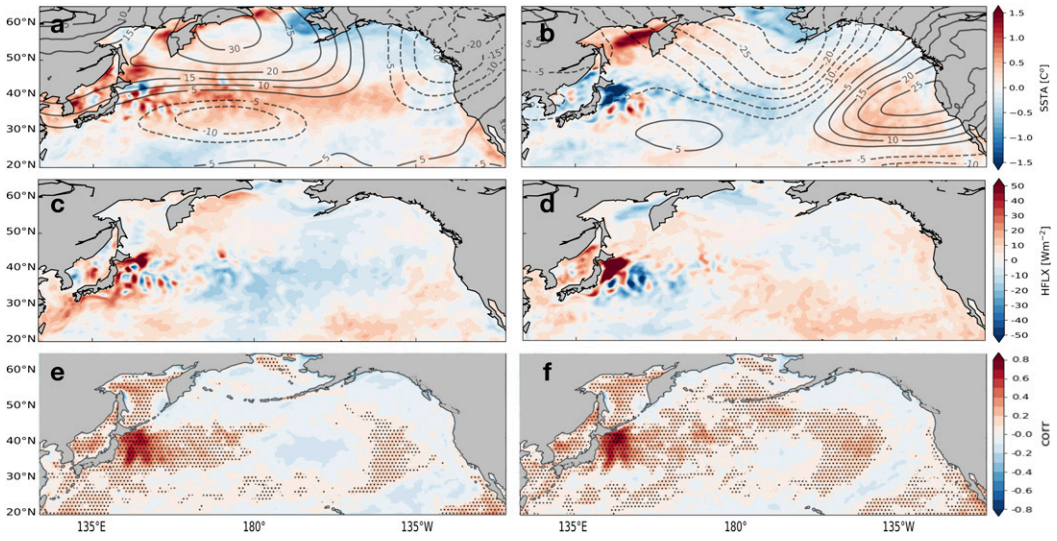

FIG. 11. Composite January–March SST (shading) and 250-hPa geopotential height (contours) anomalies for (a) inactive eddy years (IEY) and (b) active eddy years (AEY) for HR ensemble mean. Positive (negative) geopotential height anomalies shown as solid (dashed) contours. Contour interval is 5 m, and the zero contours are omitted. Composite January–March turbulent heat flux anomalies for (c) IEY and (d) AEY for HR ensemble mean. Correlation maps between January–March SST and turbulent heat flux anomalies for (e) IEY and (f) AEY HR composites. Correlations significant at 95% confidence level are shaded by dots.

high-pass-filtered (10 day) meridional wind speed variance (Chang and Fu 2002; Wettstein and Wallace 2010) between IEY and AEY. During years of reduced eddy activity and stable KE system (IEY), there is a significant southward shift in 250-hPa storm track (Figs. 12e,f) in the eastern part of the basin and both the lower- and upper-level zonal winds display a significant equatorward shift (Figs. 12c,d) compared to years of increased eddy activity (AEY). A significant deceleration of the zonal flow is also noted downstream of the KE region and near Alaska. The zonal wind anomalies in the MERRA-2 reanalysis (Fig. 12d) show a similar pattern with weakened southwest–northeast-oriented zonal winds and enhanced winds over the subarctic northwestern Pacific, although located slightly to the south, at about 30°–40°N, compared to the HR ensemble forecast in the western Pacific.

Although only the years of near-neutral phase of ENSO and PDO were considered in the composite analysis, there is a possibility that remaining SST anomalies, correlated with the

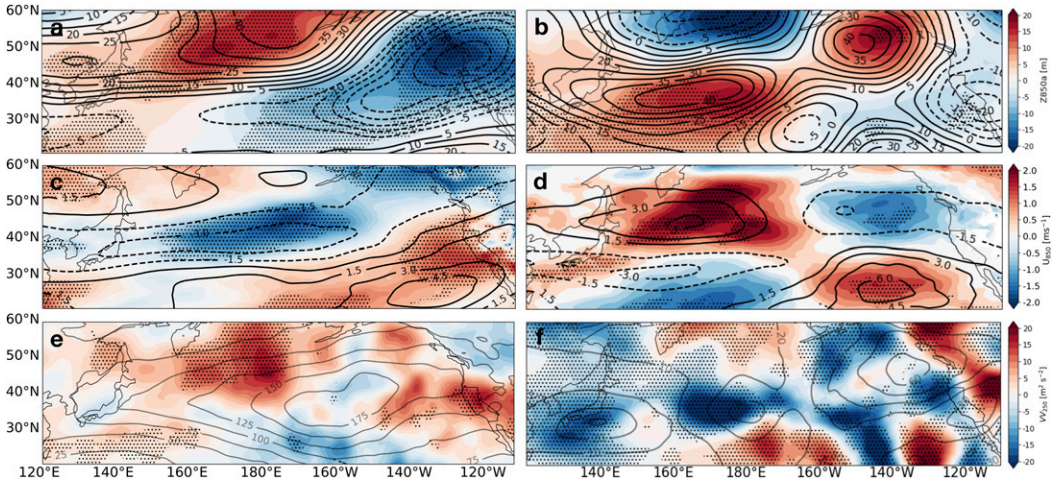

FIG. 12. Composite mean difference (IEY − AEY) in January–March: geopotential height anomalies at 250 (contours) and 850 hPa (shading) for (a) HR retrospective ensemble forecast and (b) NASA MERRA-2 reanalysis; zonal wind at 250 (contours) and 850 hPa (shading) for (c) HR and (d) MERRA-2; high-pass filtered (10 days) 250-hPa meridional velocity variance (contours show climatology) for (e) HR and (f) MERRA-2 reanalysis. Differences significant at 95% confidence level based on a two-sided Wilcoxon rank-sum test are shaded by dots.

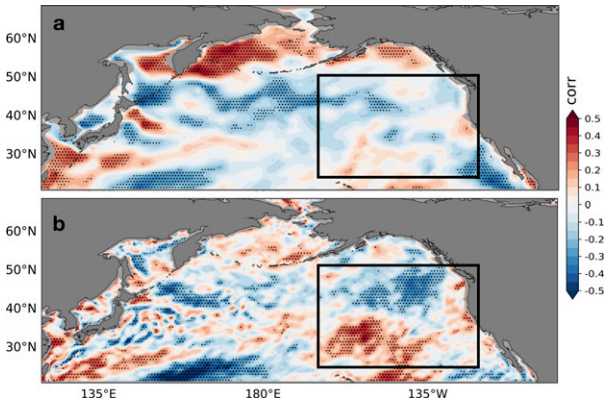

FIG. 13. Atmospheric January–March downstream wind stress curl feedback of the KE, outlined by the black box, for (a) LR retrospective forecasts and (b) HR retrospective forecasts. Shading shows the correlation maps of the 3-month low-pass wind stress curl anomalies and the KE index for lag 2 months (lagged curl anomalies vs KE index). Correlations significant at 95% confidence level are shaded by dots.

KE index, may also have an impact on the extratropical North Pacific. Figure 14 examines the SST (Figs. 14a,b) and geopotential height and precipitation anomalies (Figs. 14c,d) in the entire Indo-Pacific regions for the first 15 days of the IEY composites of both LR and HR retrospective forecasts. The results in Fig. 14 show that the composites are still associated with small SST signals in the Indian Ocean and central-western tropical Pacific as well as weak low pressure centers in the subtropical western Pacific that might be indicative of an atmospheric bridge from the tropics so that the slight contamination of the estimated response to the KE shifts cannot be excluded. Despite that, both LR and HR retrospective ensemble forecasts are similarly initialized and contain the same signal so that the difference between them for the full composites arises from the eddy-resolving features. Moreover, the existence of weak central-Pacific SST anomalies in the composites suggests that decadal climate interactions between the North Pacific western boundary current and the tropical Pacific via Pacific meridional modes may be at play.

Finally, the extent to which the low-frequency fluctuations in the KE state can influence the local atmosphere is investigated by taking a close look at vertical sections over the northern edge of the KE region where the strong SST gradient is situated. Figure 15 shows the HR and LR longitude–height sections of the vertical velocity difference (ω in isobaric levels) between AEY when the current is weakened with a meandering southerly path and IEY when the KE is strengthened with a steady and northerly path. Figure 15b shows that there is a relative decrease in the upward vertical motion over most of the KE region during AEY compared to inactive eddy years (IEY) in the LR retrospective forecast. However, in the HR forecast, when the KE is in an unstable (eddy-active) state, the overall decrease in vertical motion during AEY is disrupted by a local structure showing sharp increases in ascending motion extending to the upper troposphere (Fig. 15a). The ascending motion structure is deeper to the middle-west part of the KE region and is indicative of an active role of ocean eddies in influencing the atmosphere.

Collectively, these results in this section indicate that the insufficient resolution of the LR retrospective forecasts leads to an unrealistic simulation of the winter rainfall in the USPN region and the associated large-scale atmospheric response to the dynamic state of the KE system.

4. Summary and conclusions

We diagnosed low-frequency ocean–atmosphere variability over the North Pacific and its association with the Kuroshio Extension. Remarkably, using observations and two contrasting low- and high-resolution coupled global ensemble retrospective forecasts, we show that Kuroshio Extension variability and precipitation in western North America are intimately connected and that capturing and predicting this connection requires models that resolve the mesoscale features of the Kuroshio. The lagged cross-correlation analysis between January–March AVISO KE index (KEI) time series and the rainfall over land (36°–44°N, 235°–250°E) indicates the KEI leading the USNP rainfall by three months for MERRA-2 reanalysis, one month for HR, and two months for LR, with coefficients of 0.56, 0.6, and 0.34 respectively. The results described here are consistent with previous work showing that low-frequency variability in the Kuroshio Extension,

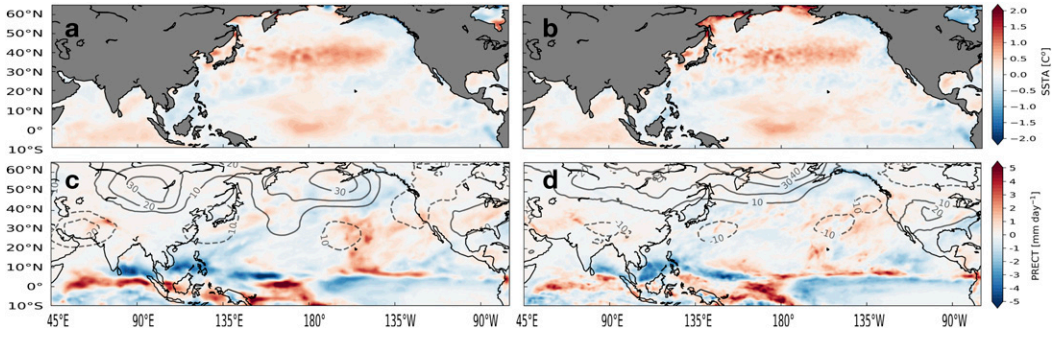

FIG. 14. (top) Sea surface temperature anomalies for the first 15 days of the IEY composites of (a) LR and (b) HR retrospective forecasts, including the Indo-Pacific regions. (bottom) Precipitation and 500-hPa geopotential height anomalies (in contours) for the first 15 days of the IEY composites of (c) LR and (d) HR retrospective forecasts.

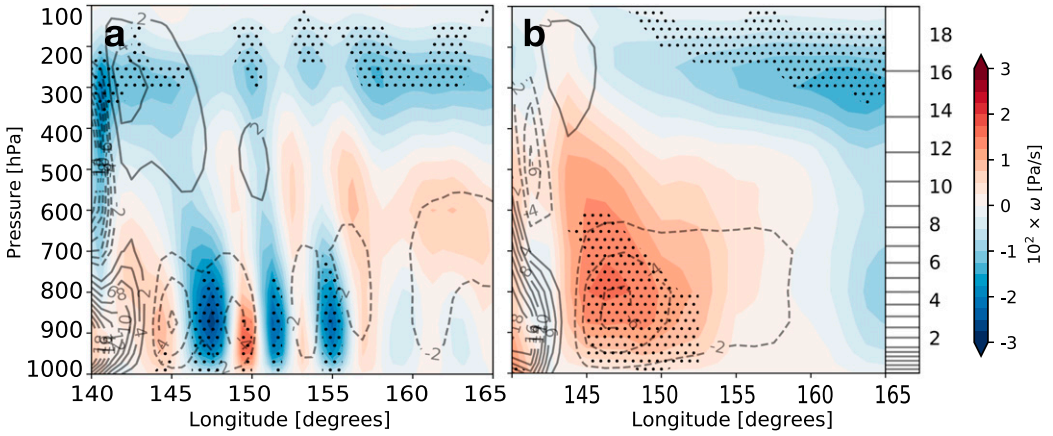

FIG. 15. January–March longitude–height section of latitudinally averaged (from 35° to 37°N) vertical velocity difference (ω positive downward) between active eddy years (AEY) and inactive eddy years (IEY) composites for the (a) HR and (b) LR ensemble mean. The IEY mean composite is overlaid in gray contours. The right y axis shows the height of vertical model layers in kilometers. Differences significant at 95% confidence level based on a two-sided Wilcoxon rank-sum test are shaded by dots.

driven by baroclinic Rossby waves carrying interior wind-forced SSH anomalies, influences the extratropical storm track across the North Pacific basin, and ultimately rainfall along the west coast of North America.

This teleconnection between the Kuroshio Extension undulations and western North American rainfall is embedded in a decadal progression in the North Pacific. Specifically, observed decadal variations involve a slow progression of a lower-tropospheric height dipole around the North Pacific and associated shifts in rainfall. We further explored the linkage between the identified atmospheric mode and the low-frequency transitions in the dynamic state of the Kuroshio Extension. We found Kuroshio Extension variability to be driven by wind-forced Rossby wave signals four years earlier in the central and eastern North Pacific. Essentially, the Kuroshio Extension oscillates between ocean eddy active regimes and ocean eddy inactive regimes with an approximately 8-yr period, and these oscillations are driven by a delayed excitation of Rossby waves in the central and eastern Pacific. The substantive details of this decadal variability are represented very differently in the ocean eddy-parameterized and ocean eddy-permitting coupled forecast systems. In particular, we find substantial differences in the storm track, lower- and upper-level zonal winds, and rainfall between the low- and high-resolution retrospective ensemble forecasts, demonstrating that resolving mesoscale ocean variability and the associated air–sea interaction is critical to capture changes in seasonal (winter) rainfall in the U.S. Pacific Northwest region and the accompanying large-scale atmospheric response to decadal variations in the dynamic state of the KE system.

The fact that the western North American precipitation teleconnection is embedded in this decadal progression is examined here primarily from the perspective of initialized predictions. The prediction framework is used because the coupled model (either eddy-resolving or eddy-parameterized) is unable to capture the multiyear evolution of the decadal progression. When initialized with observational estimates, the prediction system indicates persistence of the low-frequency state for a few seasons but does not capture the transition between states. Nevertheless, we are able, at least with the eddy-resolving model, to predict the seasonal western North American precipitation teleconnection by taking advantage of this limited seasonal persistence.

The natural follow-on question is to understand why the model fails to reproduce the decadal progression adequately. We have examined this issue in the context of eddy-parameterized and eddy-resolving multidecadal simulations, and while we do not have a clear answer, we do hypothesize that the failure is not resolution-dependent. Our preliminary analysis suggests that the limiting factor is more related to the persistence of the KE atmospheric downstream feedback in the eastern Pacific as the forcing of the subtropical Pacific SST anomalies and central tropical Pacific variability. We hypothesize that a dynamical pathway where the KE downstream ocean–atmosphere response in the eastern North Pacific—energized by the atmospheric teleconnections associated with the Pacific meridional modes and central Pacific ENSO (Joh and Di Lorenzo 2019)—plays a crucial role in the phase transitions of the KE system. We do, however, argue that capturing the ocean mesoscale features is critical in terms of predicting the downstream atmospheric precipitation teleconnection.

Acknowledgments. The authors acknowledge funding from the U.S. National Science Foundation (NSF; OCE1419569), NOAA (NA18OAR4310293, NA15OAR4320064), and DOE (DE-SC0019433). The coupled global retrospective forecasts were performed using computing resources provided by the University of Miami Center for Computational Science (UM-CCS) and by the Climate Simulation Laboratory (ark:/85065/d7wd3xhc) at NCAR's Computational and Information Systems Laboratory (NCAR-CISL), sponsored by the National Science Foundation and other agencies. The source code for the model used in this study, the NCAR CCSM4, is freely available at http://

www.cesm.ucar.edu/models/ccsm4.0 and the initial conditions from the CFSR reanalysis at https://www.ncdc.noaa.gov/data-access/model-data/model-datasets/climate-forecast-system-version2-cfsv2. The SSA-MTM toolkit was used in the M-SSA analysis and is freely available by the SSA-MTM Group at http://www.atmos.ucla.edu/tcd/ssa. We acknowledge the freely obtained atmospheric data from NASA MERRA-2 reanalysis at https://gmao.gsfc.nasa.gov/reanalysis/MERRA-2, and observed rainfall from TRMM 3B42 (https://pmm.nasa.gov/data-access/downloads/trmm) and the NOAA-CPC CMORPH_BLD V1.0 (ftp://ftp.cpc.ncep.noaa.gov/precip/CMORPH_V1.0). The PDO index was obtained from JISAO-University of Washington at http://research.jisao.washington.edu/pdo, and the ENSO(SOI) index from NOAA at https://www.esrl.noaa.gov/psd/gcos_wgsp/Timeseries/SOI). Acknowledgments are also due to the SODA3.3 ocean reanalysis data sets (http://www.atmos.umd.edu/~ocean), and to the SSALTO/DUACS altimeter products produced and distributed by the Copernicus Marine and Environment Monitoring Service (CMEMS) (http://marine.copernicus.eu).

REFERENCES

Allen, M. R., and A. W. Robertson, 1996: Distinguishing modulated oscillations from colored noise in multivariate datasets. *Climate Dyn.*, **12**, 775–784, https://doi.org/10.1007/s003820050142.

Anderson, B. T., 2019: Empirical evidence linking the Pacific decadal precession to Kuroshio Extension variability. *J. Geophys. Res. Atmos.*, **124**, 12 845–12 863, https://doi.org/10.1029/2019JD031163.

——, D. J. S. Gianotti, G. Salvucci, and J. Furtado, 2016a: Dominant timescales of potentially predictable precipitation variations across the continental United States. *J. Climate*, **29**, 8881–8897, https://doi.org/10.1175/JCLI-D-15-0635.1.

——, ——, J. Furtado, and E. Di Lorenzo, 2016b: A decadal precession of atmospheric pressures over the North Pacific. *Geophys. Res. Lett.*, **43**, 3921–3927, https://doi.org/10.1002/2016GL068206.

——, J. C. Furtado, E. Di Lorenzo, and D. J. S. Gianotti, 2017: Tracking the Pacific decadal precession. *J. Geophys. Res. Atmos.*, **122**, 3214–3227, https://doi.org/10.1002/2016JD025962.

Bif, M. B., L. Siqueira, and D. A. Hansell, 2019: Warm events induce loss of resilience in organic carbon production in the northeast Pacific Ocean. *Global Biogeochem. Cycles*, **33**, 1174–1186, https://doi.org/10.1029/2019GB006327.

Bishop, S. P., R. J. Small, F. O. Bryan, and R. A. Tomas, 2017: Scale dependence of midlatitude air–sea interaction. *J. Climate*, **30**, 8207–8221, https://doi.org/10.1175/JCLI-D-17-0159.1.

Bond, N. A., M. F. Cronin, H. Freeland, and N. Mantua, 2015: Causes and impacts of the 2014 warm anomaly in the NE Pacific. *Geophys. Res. Lett.*, **42**, 3414–3420, https://doi.org/10.1002/2015GL063306.

Bryan, F. O., R. Tomas, J. M. Dennis, D. B. Chelton, N. G. Loeb, and J. L. McClean, 2010: Frontal scale air–sea interaction in high-resolution coupled climate models. *J. Climate*, **23**, 6277–6291, https://doi.org/10.1175/2010JCLI3665.1.

Carton, J. A., G. A. Chepurin, and L. Chen, 2018: SODA3: A new ocean climate reanalysis. *J. Climate*, **31**, 6967–6983, https://doi.org/10.1175/JCLI-D-18-0149.1.

Ceballos, L., E. Di Lorenzo, C. D. Hoyos, N. Schneider, and B. Taguchi, 2009: North Pacific Gyre Oscillation synchronizes climate variability in the eastern and western boundary current systems. *J. Climate*, **22**, 5163–5174, https://doi.org/10.1175/2009JCLI2848.1.

Chang, E. K., and Y. Fu, 2002: Interdecadal variations in Northern Hemisphere winter storm track intensity. *J. Climate*, **15**, 642–658, https://doi.org/10.1175/1520-0442(2002)015<0642:IVINHW>2.0.CO;2.

Chelton, D. B., and S.-P. Xie, 2010: Coupled ocean–atmosphere interaction at the oceanic mesoscale. *Oceanography*, **23**, 52–69, https://doi.org/10.5670/oceanog.2010.05.

Chen, X., and J. M. Wallace, 2015: ENSO-like variability: 1900–2013. *J. Climate*, **28**, 9623–9641, https://doi.org/10.1175/JCLI-D-15-0322.1.

Chikamoto, Y., A. Timmermann, M. J. Widlansky, M. A. Balmaseda, and L. Stott, 2017: Multi-year predictability of climate, drought, and wildfire in southwestern North America. *Sci. Rep.*, **7**, 6568, https://doi.org/10.1038/s41598-017-06869-7.

Covey, C., C. Doutriaux, P. J. Gleckler, K. E. Taylor, K. E. Trenberth, and Y. Zhang, 2018: High-frequency intermittency in observed and model-simulated precipitation. *Geophys. Res. Lett.*, **45**, 12 514–12 522, https://doi.org/10.1029/2018GL078926.

Czaja, A., C. Frankignoul, S. Minobe, and B. Vannière, 2019: Simulating the midlatitude atmospheric circulation: What might we gain from high-resolution modeling of air–sea interactions? *Curr. Climate Change Rep.*, **5**, 390–406, https://doi.org/10.1007/s40641-019-00148-5.

Dai, A., 2012: The influence of the inter-decadal Pacific oscillation on US precipitation during 1923–2010. *Climate Dyn.*, **41**, 633–646, https://doi.org/10.1007/s00382-012-1446-5.

Deser, C., M. A. Alexander, and M. S. Timlin, 1999: Evidence for a wind-driven intensification of the Kuroshio Current Extension from the 1970s to the 1980s. *J. Climate*, **12**, 1697–1706, https://doi.org/10.1175/1520-0442(1999)012<1697:EFAWDI>2.0.CO;2.

Di Lorenzo, E. and N. Mantua, 2016: Multi-year persistence of the 2014/15 North Pacific marine heatwave. *Nature Climate Change*, **6**, 1042–1047, https://doi.org/10.1038/nclimate3082.

——, and Coauthors, 2008: North Pacific Gyre Oscillation links ocean climate and ecosystem change. *Geophys. Res. Lett.*, **35**, L08607, https://doi.org/10.1029/2007GL032838.

Drobyshev, I., Y. Bergeron, A. Vernal, A. Moberg, A. A. Ali, and M. Niklasson, 2016: Atlantic SSTs control regime shifts in forest fire activity of northern Scandinavia. *Sci. Rep.*, **6**, 22532, https://doi.org/10.1038/srep22532.

Dvoretzky, A., J. Kiefer, and J. Wolfowitz, 1956: Asymptotic minimax character of the sample distribution function and of the classical multinomial estimator. *Ann. Math. Stat.*, **27**, 642–669, https://doi.org/10.1214/aoms/1177728174.

Ebisuzaki, W., 1997: A method to estimate the statistical significance of a correlation when the data are serially correlated. *J. Climate*, **10**, 2147–2153, https://doi.org/10.1175/1520-0442(1997)010<2147:AMTETS>2.0.CO;2.

Eyring, V., S. Bony, G. A. Meehl, C. A. Senior, B. Stevens, R. J. Stouffer, and K. E. Taylor, 2016: Overview of the Coupled Model Intercomparison Project Phase 6 (CMIP6) experimental design and organization. *Geosci. Model Dev.*, **9**, 1937–1958, https://doi.org/10.5194/gmd-9-1937-2016.

Fay, M. P., and M. A. Proschan, 2010: Wilcoxon-Mann-Whitney or t-test? On assumptions for hypothesis tests and multiple interpretations of decision rules. *Stat. Surv.*, **4**, 1–39, https://doi.org/10.1214/09-SS051.

Feliks, Y., M. Ghil, and E. Simonnet, 2007: Low-frequency variability in the mid-latitude baroclinic atmosphere induced by an oceanic thermal front. *J. Atmos. Sci.*, **64**, 97–116, https://doi.org/10.1175/JAS3780.1.

——, ——, and A. W. Robertson, 2011: The atmospheric circulation over the North Atlantic as induced by the SST field. *J. Climate*, **24**, 522–542, https://doi.org/10.1175/2010JCLI3859.1.

Frankignoul, C., N. Sennéchael, Y. Kwon, and M. A. Alexander, 2011: Influence of the meridional shifts of the Kuroshio and the Oyashio Extensions on the atmospheric circulation. *J. Climate*, **24**, 762–777, https://doi.org/10.1175/2010JCLI3731.1.

Gelaro, R., and Coauthors, 2017: The Modern-Era Retrospective Analysis for Research and Applications, version 2 (MERRA-2). *J. Climate*, **30**, 5419–5454, https://doi.org/10.1175/JCLI-D-16-0758.1.

Ghil, M., and Coauthors, 2002: Advanced spectral methods for climate time series. *Rev. Geophys.*, **40**, 1003, https://doi.org/10.1029/2000RG000092.

Groth, A., Y. Feliks, D. Kondrashov, and M. Ghil, 2017: Interannual variability in the North Atlantic Ocean's temperature field and its association with the wind stress forcing. *J. Climate*, **30**, 2655–2678, https://doi.org/10.1175/JCLI-D-16-0370.1.

Hasselmann, K., 1976: Stochastic climate models part I. Theory. *Tellus*, **28**, 473–485, https://doi.org/10.3402/tellusa.v28i6.11316.

He, J., B. Kirtman, B. J. Soden, G. A. Vecchi, H. Zhang, and M. Winton, 2018: Impact of ocean eddy resolution on the sensitivity of precipitation to CO_2 increase. *Geophys. Res. Lett.*, **45**, 7194–7203, https://doi.org/10.1029/2018GL078235.

Joh, Y., and E. Di Lorenzo, 2017: Increasing coupling between NPGO and PDO leads to prolonged marine heatwaves in the northeast Pacific. *Geophys. Res. Lett.*, **44**, 11 663–11 671, https://doi.org/10.1002/2017GL075930.

——, and ——, 2019: Interactions between Kuroshio Extension and central tropical Pacific lead to preferred decadal-timescale oscillations in Pacific climate. *Sci. Rep.*, **9**, 13558, https://doi.org/10.1038/s41598-019-49927-y.

Joyce, R. J., P. Xie, Y. Yarosh, J. E. Janowiak, and P. A. Arkin, 2010: CMORPH: A "morphing" approach for high resolution precipitation product generation. *Satellite Rainfall Applications for Surface Hydrology*, M. Gebremichael and F. Hossain, Eds., Springer, 23–37.

Kelly, K. A., R. J. Small, R. M. Samelson, B. Qiu, T. M. Joyce, Y. Kwon, and M. F. Cronin, 2010: Western boundary currents and frontal air–sea interaction: Gulf Stream and Kuroshio Extension. *J. Climate*, **23**, 5644–5667, https://doi.org/10.1175/2010JCLI3346.1.

Kirtman, B. P., and D. Min, 2009: Multimodel ensemble ENSO prediction with CCSM and CFS. *Mon. Wea. Rev.*, **137**, 2908–2930, https://doi.org/10.1175/2009MWR2672.1.

——, and Coauthors, 2012: Impact of ocean model resolution on CCSM climate simulations. *Climate Dyn.*, **39**, 1303–1328, https://doi.org/10.1007/s00382-012-1500-3.

——, and Coauthors, 2013: Near-term climate change: Projections and predictability. *Climate Change 2013: The Physical Science Basis*, T. F. Stocker et al., Eds., Cambridge University Press, 955–1028.

——, and Coauthors, 2014: The North American Multi-Model Ensemble (NMME): Phase-1 seasonal-to-interannual prediction; Phase-2 toward developing intra-seasonal prediction. *Bull. Amer. Meteor. Soc.*, **95**, 585–601, https://doi.org/10.1175/BAMS-D-12-00050.1.

Kushnir, Y., and Coauthors, 2019: Towards operational predictions of the near-term climate. *Nat. Climate Change*, **9**, 94–101, https://doi.org/10.1038/s41558-018-0359-7.

Kwon, Y., M. A. Alexander, N. A. Bond, C. Frankignoul, H. Nakamura, B. Qiu, and L. A. Thompson, 2010: Role of the Gulf Stream and Kuroshio–Oyashio systems in large-scale atmosphere–ocean interaction: A review. *J. Climate*, **23**, 3249–3281, https://doi.org/10.1175/2010JCLI3343.1.

Latif, M., and T. P. Barnett, 1994: Causes of decadal climate variability over the North Pacific and North America. *Science*, **266**, 634–637, https://doi.org/10.1126/science.266.5185.634.

Laurindo, L. C., L. Siqueira, A. J. Mariano, and B. J. Kirtman, 2019: Cross-spectral analysis of the SST/10-m wind speed coupling resolved by satellite products and climate model simulations. *Climate Dyn.*, **52**, 5071–5098, https://doi.org/10.1007/s00382-018-4434-6.

Linkin, M. E., and S. Nigam, 2008: The North Pacific Oscillation–west Pacific teleconnection pattern: Mature-phase structure and winter impacts. *J. Climate*, **21**, 1979–1997, https://doi.org/10.1175/2007JCLI2048.1.

Ma, X., and Coauthors, 2015: Distant influence of Kuroshio eddies on North Pacific weather patterns? *Sci. Rep.*, **5**, 17785, https://doi.org/10.1038/srep17785.

——, P. Chang, R. Saravanan, R. Montuoro, H. Nakamura, D. Wu, X. Lin, and L. Wu, 2017: Importance of resolving Kuroshio front and eddy influence in simulating the North Pacific storm track. *J. Climate*, **30**, 1861–1880, https://doi.org/10.1175/JCLI-D-16-0154.1.

Malone, R., R. Smith, R. Maltrud, and M. Hecht, 2003: Eddy-resolving ocean modeling. *Los Alamos Sci.*, **28**, 223–231.

Maltrud, M. E., R. D. Smith, A. J. Semtner, and R. C. Malone, 1998: Global eddy resolving ocean simulations driven by 1985–1994 atmospheric winds. *J. Geophys. Res.*, **103**, 30 825–30 853, https://doi.org/10.1029/1998JC900013.

Mantua, N., S. R. Hare, Y. Zhang, J. M. Wallace, and R. C. Francis, 1997: A Pacific interdecadal climate oscillation with impacts on salmon production. *Bull. Amer. Meteor. Soc.*, **78**, 1069–1079, https://doi.org/10.1175/1520-0477(1997)078<1069:APICOW>2.0.CO;2.

Marzocchi, A., J. J.-M. Hirschi, N. P. Holliday, S. A. Cunningham, A. T. Blaker, A. C. Coward, 2015: The North Atlantic subpolar circulation in an eddy-resolving global ocean model. *J. Mar. Syst.*, **142**, 126–143, https://doi.org/10.1016/j.jmarsys.2014.10.007.

McCarthy, G. D., T. M. M. Joyce, and S. A. Josey, 2018: Gulf Stream variability in the context of quasi-decadal and multi-decadal Atlantic climate variability. *Geophys. Res. Lett.*, **45**, 11 257–11 264, https://doi.org/10.1029/2018GL079336.

Meehl, G. A., G. J. Boer, C. Covey, M. Latif, and R. J. Stouffer, 2000: The Coupled Model Intercomparison Project (CMIP). *Bull. Amer. Meteor. Soc.*, **81**, 313–318, https://doi.org/10.1175/1520-0477(2000)081<0313:TCMIPC>2.3.CO;2.

Minobe, S., A. Kuwano-Yoshida, N. Komori, S.-P. Xie, and R. J. Small, 2008: Influence of the Gulf Stream on the troposphere. *Science*, **452**, 206–209, https://doi.org/10.1038/nature06690.

Na, H., K. Kim, S. Minobe, and Y. N. Sasaki, 2018: Interannual to decadal variability of the upper-ocean heat content in the western North Pacific and its relationship to oceanic and atmospheric variability. *J. Climate*, **31**, 5107–5125, https://doi.org/10.1175/JCLI-D-17-0506.1.

Newman, M., and Coauthors, 2016: The Pacific decadal oscillation, revisited. *J. Climate*, **29**, 4399–4427, https://doi.org/10.1175/JCLI-D-15-0508.1.

Nigam, S., A. Ruiz-Barradas, and L. Chafik, 2018: Gulf Stream excursions and sectional detachments generate the decadal pulses in the Atlantic multidecadal oscillation. *J. Climate*, **31**, 2853–2870, https://doi.org/10.1175/JCLI-D-17-0010.1.

O'Reilly, C. H., and A. Czaja, 2015: The response of the Pacific storm track and atmospheric circulation to Kuroshio Extension variability. *Quart. J. Roy. Meteor. Soc.*, **141**, 52–66, https://doi.org/10.1002/qj.2334.

Paolino, D. A., J. L. Kinter, B. P. Kirtman, D. Min, and D. M. Straus, 2012: The impact of land surface and atmospheric

initialization on seasonal forecasts with CCSM. *J. Climate*, **25**, 1007–1021, https://doi.org/10.1175/2011JCLI3934.1.

Piazza, M., L. Terray, J. Boé, E. Maisonnave, and E. Sanchez-Gomez, 2015: Influence of small-scale North Atlantic sea surface temperature patterns on the marine boundary layer and free troposphere: A study using the atmospheric ARPEGE model. *Climate Dyn.*, **46** 1699–1717, https://doi.org/10.1007/s00382-015-2669-z.

Power, S., T. Casey, C. Folland, A. Colman, and V. Mehta, 1999: Inter-decadal modulation of the impact of ENSO on Australia. *Climate Dyn.*, **15**, 319–324, https://doi.org/10.1007/s003820050284.

Qiu, B., and S. M. Chen, 2005: Variability of the Kuroshio Extension jet, recirculation gyre, and mesoscale eddies on decadal time scales. *J. Phys. Oceanogr.*, **35**, 2090–2103, https://doi.org/10.1175/JPO2807.1.

——, N. Schneider, and S. Chen, 2007: Coupled decadal variability in the North Pacific: An observationally constrained idealized model. *J. Climate*, **20**, 3602–3620, https://doi.org/10.1175/JCLI4190.1.

——, S. Chen, N. Schneider, and B. Taguchi, 2014: A coupled decadal prediction of the dynamic state of the Kuroshio Extension system. *J. Climate*, **27**, 1751–1764, https://doi.org/10.1175/JCLI-D-13-00318.1.

Révelard, A., C. Frankignoul, N. Senneìchael, Y. O. Kwon, and B. Qiu, 2016: Influence of the decadal variability of the Kuroshio Extension on the atmospheric circulation in the cold season. *J. Climate*, **29**, 2123–2144, https://doi.org/10.1175/JCLI-D-15-0511.1.

Rivière, G., 2009: Effect of latitudinal variations in low-level baroclinicity on eddy life cycles and upper-tropospheric wave breaking processes. *J. Atmos. Sci.*, **66**, 1569–1592, https://doi.org/10.1175/2008JAS2919.1.

Roberts, M. J., H. T. Hewitt, P. Hyder, D. Ferreira, S. A. Josey, M. Mizielinski, and A. Shelly, 2016: Impact of ocean resolution on coupled air–sea fluxes and large-scale climate. *Geophys. Res. Lett.*, **43**, 10 430–10 438, https://doi.org/10.1002/2016GL070559.

Robson, J., I. Polo, D. L. R. Hodson, D. P. Stevens, and L. C. Shaffrey, 2018: Decadal prediction of the North Atlantic subpolar gyre in the HiGEM high-resolution climate model. *Climate Dyn.*, **50**, 921–937, https://doi.org/10.1007/s00382-017-3649-2.

Ropelewski, C. F., and P. D. Jones, 1987: An extension of the Tahiti–Darwin Southern Oscillation Index. *Mon. Wea. Rev.*, **115**, 2161–2165, https://doi.org/10.1175/1520-0493(1987)115<2161:AEOTTS>2.0.CO;2.

Saha, S., and Coauthors, 2010: The NCEP Climate Forecast System Reanalysis. *Bull. Amer. Meteor. Soc.*, **91**, 1015–1058, https://doi.org/10.1175/2010BAMS3001.1.

Santoso, A., M. J. Mcphaden, and W. Cai, 2017: The defining characteristics of ENSO extremes and the strong 2015/2016 El Niño. *Rev. Geophys.*, **55**, 1079–1129, https://doi.org/10.1002/2017RG000560.

Sasaki, Y. N., and N. Schneider, 2011: Decadal shifts of the Kuroshio Extension jet: Application of thin-jet theory. *J. Phys. Oceanogr.*, **41**, 979–993, https://doi.org/10.1175/2011JPO4550.1.

——, S. Minobe, and N. Schneider, 2014: Decadal response of the Kuroshio Extension jet to Rossby waves: Observation and thin-jet theory. *J. Phys. Oceanogr.*, **43**, 442–456, https://doi.org/10.1175/JPO-D-12-096.1.

Schneider, N., A. J. Miller, and D. W. Pierce, 2002: Anatomy of North Pacific decadal variability. *J. Climate*, **15**, 586–605, https://doi.org/10.1175/1520-0442(2002)015<0586:AONPDV>2.0.CO;2.

Seager, R., Y. Kushnir, N. H. Naik, M. A. Cane, and J. Miller, 2001: Wind-driven shifts in the latitude of the Kuroshio–Oyashio Extension and generation of SST anomalies on decadal timescales. *J. Climate*, **14**, 4249–4265, https://doi.org/10.1175/1520-0442(2001)014<4249:WDSITL>2.0.CO;2.

——, M. Hoerling, S. Schubert, H. Wang, B. Lyon, A. Kumar, J. Nakamura, N. Henderson, 2015: Causes of the 2011–14 California drought. *J. Climate*, **28**, 6997–7024, https://doi.org/10.1175/JCLI-D-14-00860.1.

Siqueira, L., and B. P. Kirtman, 2016: Atlantic near-term climate variability and the role of a resolved Gulf Stream. *Geophys. Res. Lett.*, **43**, 3964–3972, https://doi.org/10.1002/2016GL068694.

Small, R. J., and Coauthors, 2008: Air–sea interaction over ocean fronts and eddies. *Dyn. Atmos. Oceans*, **45**, 274–319, https://doi.org/10.1016/j.dynatmoce.2008.01.001.

——, F. O. Bryan, S. P. Bishop, and R. A. Tomas, 2019: Air–sea turbulent heat fluxes in climate models and observational analyses: What drives their variability? *J. Climate*, **32**, 2397–2421, https://doi.org/10.1175/JCLI-D-18-0576.1.

Smirnov, D., M. Newman, M. A. Alexander, Y. Kwon, and C. Frankignoul, 2015: Investigating the local atmospheric response to a realistic shift in the Oyashio sea surface temperature front. *J. Climate*, **28**, 1126–1147, https://doi.org/10.1175/JCLI-D-14-00285.1.

Stocker, T. F., and Coauthors, 2013: Technical summary. *Climate Change 2013: The Physical Science Basis*, T. F. Stocker et al., Eds., Cambridge University Press, 33–115, https://doi.org/10.1017/CBO9781107415324.

Sugimoto, S., K. Aono, and S. Fukui, 2017: Local atmospheric response to warm mesoscale ocean eddies in the Kuroshio–Oyashio confluence region. *Sci. Rep.*, **7**, 11871, https://doi.org/10.1038/s41598-017-12206-9.

Swain, D. L., M. Tsiang, M. Haugen, D. Singh, A. Charland, B. Rajaratnam, and N. S. Diffenbaugh, 2014: The extraordinary California drought of 2013/14: Character, context and the role of climate change. *Bull. Amer. Meteor. Soc.*, **95**, S3–S7.

——, D. E. Horton, D. Singh, and N. S. Diffenbaugh, 2016: Trends in atmospheric patterns conducive to seasonal precipitation and temperature extremes in California. *Sci. Adv.*, **2**, e1501344, https://doi.org/10.1126/sciadv.1501344.

Taguchi, B., S.-P. Xie, N. Schneider, M. Nonaka, H. Sasaki, and Y. Sasai, 2007: Decadal variability of the Kuroshio Extension: Observations and an eddy-resolving model hindcast. *J. Climate*, **20**, 2357–2377, https://doi.org/10.1175/JCLI4142.1.

Taylor, K. E., R. J. Stouffer, and G. A. Meehl, 2012: An overview of CMIP5 and the experiment design. *Bull. Amer. Meteor. Soc.*, **93**, 485–498, https://doi.org/10.1175/BAMS-D-11-00094.1.

Teng, H., and G. Branstator, 2011: Initial-value predictability of prominent modes of North Pacific subsurface temperature in a CGCM. *Climate Dyn.*, **36**, 1813–1834, https://doi.org/10.1007/s00382-010-0749-7.

Trenberth, K. E., and J. W. Hurrell, 1994: Decadal atmosphere–ocean variations in the Pacific. *Climate Dyn.*, **9**, 303–319, https://doi.org/10.1007/BF00204745.

Volkov, D. L., T. Lee, and L. L. Fu, 2008: Eddy-induced meridional heat transport in the ocean. *Geophys. Res. Lett.*, **35**, L20601, https://doi.org/10.1029/2008GL035490.

Walraven, R., 1980: Digital filters. *Proc. Digital Equipment Computer Users Society*, San Diego, CA, Digital Equipment Corporation, 827–834.

Wang, H., and S. Schubert, 2014: Causes of the extreme dry conditions over California during early 2013 [in "Explaining Extremes of 2013 from a Climate Perspective"]. *Bull. Amer. Meteor. Soc.*, **95**, S7–S10.

Wettstein, J. J., and J. M. Wallace, 2010: Observed patterns of month-to-month storm-track variability and their relationship to the background flow. *J. Atmos. Sci.*, **67**, 1420–1437, https://doi.org/10.1175/2009JAS3194.1.

Wheeler, M. C., and H. H. Hendon, 2004: An all-season real-time multivariate MJO index: Development of an index for monitoring and prediction. *Mon. Wea. Rev.*, **132**, 1917–1932, https://doi.org/10.1175/1520-0493(2004)132<1917:AARMMI>2.0.CO;2.

Wills, R. C., T. Schneider, J. M. Wallace, D. S. Battisti, and D. L. Hartmann, 2018: Disentangling global warming, multidecadal variability, and El Niño in Pacific temperatures. *Geophys. Res. Lett.*, **45**, 2487–2496, https://doi.org/10.1002/2017GL076327.

Wu, R., B. P. Kirtman, and K. Pegion, 2006: Local air–sea relationship in observations and model simulations. *J. Climate*, **19**, 4914–4932, https://doi.org/10.1175/JCLI3904.1.

Zhou, G., M. Latif, R. J. Greatbatch, and W. Park, 2015: Atmospheric response to the North Pacific enabled by daily sea surface temperature variability. *Geophys. Res. Lett.*, **42**, 7732–7739, https://doi.org/10.1002/2015GL065356.